

Special
Collection

An Efficient Approach for Quantifying the Mechanical Degradation of Ni-Rich NMC-based Cathodes for Lithium-Ion Batteries using Nano-XCT Analysis

Daniel Goldbach,^[a, c] Jürgen Gluch,^[b] Tanja Graf,^[a] Michael Gaus,^[a] Stefan Käbitz,^[a] Michael Zillmer,^[a] and Ulrike Krewer^{*[c]}

LiNi_{0.8}Co_{0.1}Mn_{0.1}O₂ has emerged as a promising electrode material for automotive lithium-ion batteries due to its high specific discharge capacity, cost-effectiveness, and reduced cobalt content. However, despite all mentioned beneficial attributes, the widespread adoption of this material class is impeded by active material degradation during cycling operation, which is linked to performance loss. This study compares scanning electron microscopy images and nano X-ray computed tomography scans with a 3D reconstruction of pristine and cycle-aged battery electrodes to determine structural changes over cycle life. Although a very moderate current rate was chosen for the cycle test, which suggests a homogeneous

load across the entire electrode, particle fracture varied across electrode thickness and particle size. A quantitative analysis of the active material's gray scale value distribution reveals severe degradation near the separator interface with a reciprocal relationship to particle radius. Remarkably, particle shape and size remain relatively unchanged despite cracking, eliminating the need to adjust these parameters in aging simulations. Moreover, it underscores the practical significance of particle cracking, as it can significantly impact the electrode's performance. Thus, analyzing changes in particle shape and size alone is insufficient, and a comprehensive exploration of the particle interior using nano-XCT is necessary.

Introduction

Lithium-ion batteries play a crucial role as energy storage technology in portable electronic devices and electric vehicles, contributing to the reduction of reliance on fossil fuel sources.^[1,2] The widespread deployment of Ni-rich layered Lithium-Nickel-Manganese-Cobalt-Oxide (NMC) materials holds great promise for enhancing specific capacity, power capabilities, cost efficiency, and reducing the dependency on scarce cobalt resources. These advancements are pivotal for the adoption of environmentally sustainable transportation solutions, especially in cases where space for energy storage systems is limited, and range is a critical factor.^[3,4] However, the

practical application of nickel-rich NMC cathode materials faces challenges associated with degradation mechanisms that limit the operational cycle life. Among these mechanisms, intergranular fracture of cathode particles caused by significant volumetric changes during electrochemical cycling is recognized as a primary technical factor in polycrystalline materials.^[5] Consequently, this fracture can lead to the detachment of primary particles from the secondary particle matrix, enabling the penetration of liquid electrolyte into the particle interior. This, in turn, results in additional surface degradation at the cathode-electrolyte interface, leading to capacity loss and increased impedance.^[6,7]

X-ray imaging techniques with nm scale spatial resolution and compositional sensitivity, coupled with advanced computational methods for quantification, have proven to be non-invasive, effective, and informative in tracking morphological changes in materials.^[8,9] Over the past decade, this technique has garnered significant interest in the research community and has proven to be a robust tool for electrochemical materials development. It provides both visual and quantitative access to 3D morphological information on battery materials and electrode architectures.^[10–12] Depending on the resolution of the computed tomography (CT), we can investigate nanoscale particles with resolutions as fine as ten nanometers or examine the main electrode with a broad observation range spanning from a few nanometers to 1 mm, facilitated by micro-CT techniques.^[13] For instance, recent employment of nano X-ray computed tomography (nano-XCT) techniques has enabled the material-level examination of phase spatial distribution,^[14] microstructure properties like tortuosity,^[15] pore and particle size distribution^[16] and surface roughness,^[17] as well as active

[a] D. Goldbach, Dr. T. Graf, Dr. M. Gaus, Dr. S. Käbitz, Dr. M. Zillmer
Volkswagen AG
Industriestraße Nord 1, 38239 Salzgitter (Germany)

[b] Dr. J. Gluch
Fraunhofer Institute for Ceramic Technologies and Systems IKTS
Maria-Reiche-Straße 2, 01109 Dresden (Germany)

[c] D. Goldbach, Prof. Dr.-Ing. U. Krewer
Institute for Applied Materials – Electrochemical Technologies
Karlsruhe Institute of Technology
Adenauerring 20b, 76131 Karlsruhe (Germany)
E-mail: ulrike.krewer@kit.edu

Supporting information for this article is available on the WWW under
<https://doi.org/10.1002/celec.202300353>

This publication is part of a Special Collection on Holistic Development of Electrochemical Processes for Industrial Systems

© 2023 The Authors. ChemElectroChem published by Wiley-VCH GmbH. This is an open access article under the terms of the Creative Commons Attribution License, which permits use, distribution and reproduction in any medium, provided the original work is properly cited.

material degradation.^[18–20] However, these approaches are often complex to implement and require high computational power.^[21] To evaluate mechanical degradation, Rahe et al. conducted nano-meter resolution computed tomography analysis of pristine and cyclically aged NMC-based cathode samples, qualitatively observing internal crack formation within the active material particles.^[20] However, quantitative characterization and description of these cracks were not provided. In a study by Yang et al., a combination of X-ray phase contrast nano tomography, transmission X-ray microscopy, and transmission electron microscopy was employed to systematically investigate the morphological and chemical degradation of a polycrystalline NMC composite electrode content under fast charging conditions.^[10] Notably, the examined active material particles in this study exhibited a constant particle size distribution, limiting the ability to investigate crack formation across different particle sizes, as typically found in state-of-the-art battery cells used in automotive applications to achieve higher energy density through improved packing density. Jiang et al. employed an X-ray imaging method coupled with machine learning support to investigate the evolving (de)attachment of particles to the conductive matrix in an NMC-based electrode.^[22] The study also identified crack formation within the active material particles, but did not quantitatively assess them or analyze their positional relationships within the electrode. Furthermore, these studies did not compare the degraded electrode with a pristine sample and focused only on analyzing defects such as cracks, omitting an examination of particle geometry.

To address the limitations of existing research, we combine nano-XCT with an easy-to-implement systematic approach to quantify and visualize the degree of local morphological degradation in polycrystalline nickel-rich layered NMC-based cathode active material (CAM). The quantitative results are in good agreement with the qualitative observations from scanning electron microscopy (SEM) images and offer an analytical method for probing and understanding the heterogeneous particle utilization and fading during cycling operation. By streamlining the quantitative evaluation process to focus on essential information, we enable efficient and effective analysis, facilitating the comparison of a large number of samples. This capability is particularly valuable for evaluating various optimization approaches in active material formulation or electrode design, as well as operating parameters, in terms of their impact on the mechanical degradation of NMC-based cathodes.

The assumption of ideal spherical particles in simplified microstructure models may not accurately represent the morphological changes observed in aged cathode particles, as highlighted by Xu et al. and Lu et al.^[9,23] Here, our study aims to quantitatively investigate the impact of mechanical degradation during cyclic operation on particle shape. Our goal is to provide a more precise characterization of the actual state of the particles. Hence, we pay careful attention to crucial parameters such as sphericity, crack density, position within the electrode, and particle size. We deliberately distinguish between degradation occurring in the particle interior and external geometric changes. The presented methods are applied to both a pristine

and a cyclically aged $\text{LiNi}_{0.8}\text{Co}_{0.1}\text{Mn}_{0.1}\text{O}_2$ (NMC811) cathode sample, enabling a thorough before-after comparison. Notably, to the best of our knowledge, this study represents the first analysis of its kind, comparing a pristine electrode sample with a cyclically aged counterpart, while thoroughly assessing and discussing characteristic geometric properties of active material particles using a simplified evaluation of nano-XCT scans. Our study contributes to enhance the understanding of particle degradation under different aging conditions. Moreover, with our systematic quantification method, we provide researchers with a reliable tool for the design and optimization of battery active materials, facilitating the development of more reliable and high-performance energy storage systems.

Results and Discussion

The presented findings offer a comparative analysis of the mechanical damage within CAM particles between an initial pristine state and a cyclically aged NMC electrode sample. Initial qualitative comparisons are facilitated through SEM images of cross-sections from both electrode samples. Utilizing nano-XCT, a complete dataset comprising 801 images was obtained (see Figure 1(a)). This high-resolution X-ray CT imaging covered the electrode samples across the electrode thickness, offering intricate insights into electrode morphology. The acquired images were amalgamated into a three-dimensional electrode reconstruction, as illustrated in Figure 1(b–c). A 3D distance transform watershed algorithm was employed to segment individual particles within the reconstructed CAM volume, as shown in Figure 1(d), facilitating particle level specific evaluations. Particle volume and equivalent particle radius were then determined for each particle, assuming a spherical geometry. A 2D slice of the reconstructed CT scan across the electrode thickness is presented in Figure 1(e), depicting the current collector and CAM particles with varying fracture degrees. The gray scale value within CT data corresponding to voxels containing small cracks appears darker, differentiating them from denser CAM regions. To render this information on cracks within the CAM amenable for quantitative analysis, gray scale values of tomography images are utilized. These values, scaled between 0 and 255, provide an indication of crack density. Darker gray scale values within the CAM portion correspond to a higher proportion of cracks, which in turn results in an increased mean gray value for the particle. To standardize comparisons and minimize the impact of factors like illumination on CT scans, the mean gray scale value of each CAM particle is normalized by averaged mean gray scale value of the three densest CAM particles within the sample volume, and hereafter referred to as the CAM damage variable Γ_i . This method guarantees the selection of particles with minimal internal pores or cracks as a reference for dense CAM. With the heuristic algorithm introduced in this work, all particles are evaluated based on the mean gray scale value of these reference particles. Particularly small particles, lacking cracks or pores, serve as a reliable reference. The degree of cracking is quantified for each particle by the CAM damage variable Γ_i ,

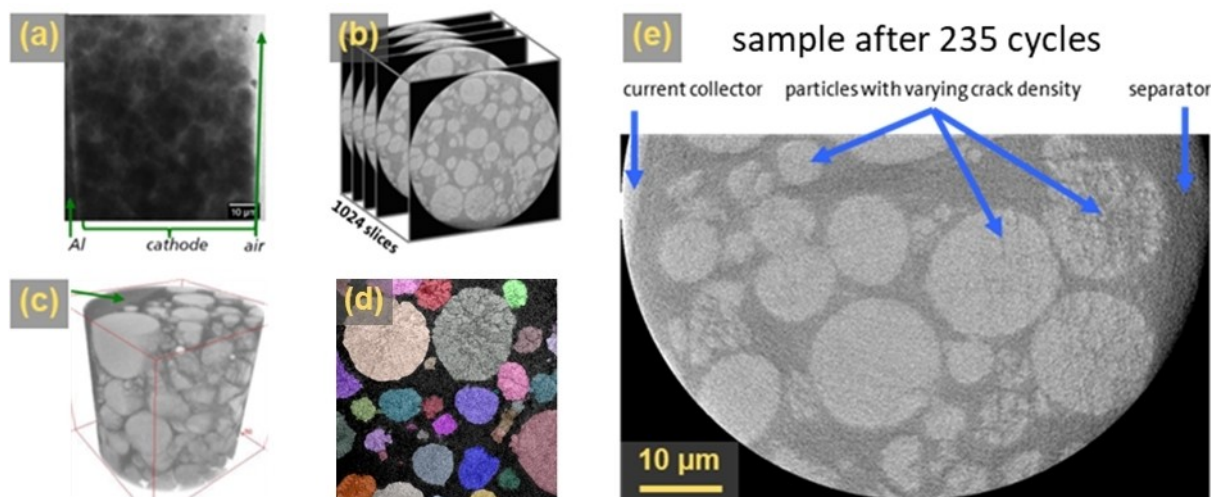


Figure 1. Illustration of nano-XCT analysis and image processing using an NMC811 electrode sample after 235 cycles. (a) Tomography scan of the electrode, (b) 2D slices of the 3D-reconstruction of the tomography data, (c) Full field of view of the 3D-reconstruction, (d) Segmentation of individual particles using the watershed algorithm, depicted with distinct colors. This segmentation is overlaid onto the unsegmented gray scale data, visualized in 2D slices of the 3D reconstruction. (e) Excerpt of a 2D slice of the 3D-reconstruction showing particles with different crack densities.

ranging from zero (reflecting the baseline value for densely packed CAM with minimal indications of crack formation within the electrode sample) to one (indicating the uppermost theoretical limit for potential crack formation). The variable Γ_i , introduced as a proxy value, precisely evaluates a particle's damage relative to the three densest reference particles. This approach simplifies crack-related damage comparison across particles and electrode samples, aiding in easy interpretation. A comprehensive description of the calculation and thorough discussion of this introduced method is elaborated upon in the experimental section.

Additionally, a thorough analysis of particle shape was undertaken, drawing on established definitions by Walz, Lu et al., and Wadell.^[23–25] To quantitatively characterize the shape of the particles, a method proposed by Walz suggests determining their dimensions in three mutually perpendicular spatial coordinates.^[24] These dimensions are denoted as x_a (long axis), x_b (middle axis) and x_c (short axis) subsequently. By calculating the ratios x_a/x_c and x_b/x_c , individual particles or particle aggregates can be classified into categories such as spherical, cylindrical, sheets, or intermediate forms, as presented in the results section. However, this approach primarily focuses on the compactness of the particles and does not fully capture their sphericity. To address this limitation, we incorporate two definitions from the literature to assess the sphericity of both pristine and aged particles.^[23,25] The results of these comparisons are thoroughly examined and discussed in the subsequent section.

Sphericity definition according to Lu et al. (Eq. 1):^[23]

$$\Psi_{Lu} = \frac{\text{length short axis}}{\text{length long axis}} = \frac{x_c}{x_a} \quad (1)$$

Sphericity definition according to Wadell (Eq. 2):^[25]

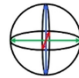
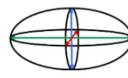
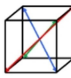
$$\Psi_{Wadell} = \frac{\text{surface of sphere with same volume}}{\text{actual surface}} \quad (2)$$

A general comparison of the two definitions based on simplified geometries is shown in Table 1. This comparative analysis, grounded in established metrics, was designed to illuminate particle shape and geometry. By integrating these metrics into our investigation, we aimed to enhance the overall comprehension of particle transformations throughout the cycling process.

Electrochemical cycling

To investigate the mechanical degradation of the NMC under repeated cyclic charging/discharging, a cathode half-cell was subjected to 235 cycles and compared to a pristine cathode

Table 1. Comparison of the sphericity according to Lu et al.^[23] and Wadell^[25] for three exemplary geometries with unit length 1 (sphere, ellipsoid and cube).

			
	sphere	ellipsoid	cube
x_a	1	2	1
x_b	1	1	1
x_c	1	1	1
actual surface	π	≈ 4.9870	≈ 2.8845
surface of sphere with same volume	π	≈ 5.3649	≈ 3.4499
Ψ_{Lu}	1	0.5	1
Ψ_{Wadell}	1	0.9296	0.8361

sample. The cell configuration included a large electrolyte amount of 200 μL and a 260 μm thick glass fiber separator, serving as an electrolyte reservoir. Additionally, a Li metal counter-electrode was employed to ensure a surplus of Li in the system. Due to the overdesign of these components, the observed capacity loss can be attributed to the cathode sample. A slow discharge capacity test conducted at a low current rate of C/20 revealed a discharge capacity of 2.93 mAh cm^{-2} before the cycle test, which decreased to 1.31 mAh cm^{-2} after the test. Since kinetic limitations are minimal at such a low current rate, overpotentials are negligible. Thus, the difference in discharge capacity of 1.62 mAh cm^{-2} (–55.4%) before and after the cycle test can be roughly attributed to a loss of active Li storage sites in the CAM. Possible causes for this loss include contact loss of CAM particle fragments resulting from particle cracks or irreversible phase transformation of the CAM into an electrochemically inactive rock salt phase in the near-surface region of the particles. The first cycle of the experiment exhibited a 9.6% difference between the discharge capacity at C/2 and the slow discharge test capacity at C/20, while after 235 cycles, this difference increased to 42.6%. This increase is likely attributed to heightened overpotentials resulting from an increased cathode resistance. The investigated cycle-aged CAM electrode sample exhibited a capacity loss of 55.4%, falling below the typical end-of-service criterion of 50% residual capacity for lithium-ion battery applications. Thus, the presented method and interpretation of results can be directly applied to relevant aging states between the examined conditions. Since the analysis of the electrochemical performance is not the focus of this work, further details on the electrical data of the cycle test are presented in the appendix.

Scanning electron microscopy

The SEM image of the pristine electrode sample depicted in Figure 2(a) reveals noticeable gaps between the NMC particles, indicating that the electrode was only slightly calendared. Consequently, the pristine electrode exhibits only very few visible cracks along the grain boundaries of the secondary particles, making it highly suitable for crack investigations. In contrast, the active material particles of the cycle-aged electrode sample shown in Figure 2(b) exhibit severe crack formation throughout the entire electrode thickness. Additionally, it is evident that cracks increase in density and width as the distance from the current collector (bottom) increases, with the most significant occurrence observed at the separator interface (top). Calendaring of battery electrodes involves the application of high pressure, which varies depending on battery type, electrode material, and manufacturing method. Typical calendaring pressures can reach several thousand kPa or even higher. To calculate the pressure exerted on the electrode in the cell setup, the force applied to the electrode surface is divided by the surface area. In the case of the PAT-Core cell setup, a clamping force of 40 N is applied to the electrode, which has a diameter of 18 mm, resulting in a surface area of 2.5434 cm^2 . Thus, the pressure can be determined as follows: Pressure =

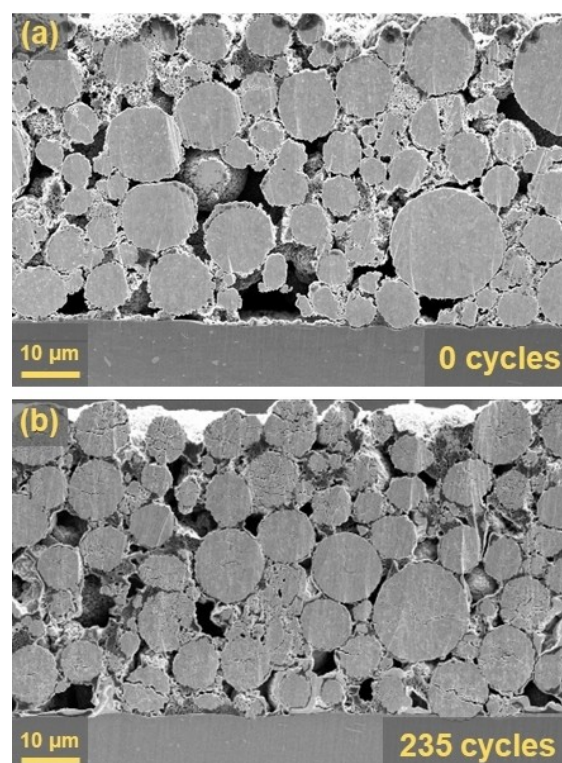


Figure 2. Scanning electron microscopy images for electrodes considered in this work (separator interface at the top, current collector at the bottom). (a) pristine electrode with 0 cycles, (b) cycle aged electrode after 235 cycles.

$40 \text{ N} / 0.00025434 \text{ m}^2 \approx 157,229 \text{ Pa}$. The pressure exerted on the electrode in the PAT-Core cell due to tension is significantly lower than the typical calendaring pressure. This indicates that further compression of the electrode material or crack formation is not expected during cell assembly. These findings support the conclusion that the formation of secondary particle fractions observed in previous cyclic aging studies on Ni-rich cathodes is primarily attributed to the stress developed during repeated charging and discharging.^[5,6,26]

Nano-XCT analysis

In order to further investigate the influence of particle size and location within the electrode on crack formation, nano-XCT measurements were conducted. The nano-XCT images, as depicted in Figure 1(e), allow for the identification of structural changes in the cathode, including particle cracking. Cracks within the CAM result in lower gray scale values on a scale ranging from 0 to 255. As mentioned previously, the mean gray scale value of the electrode reconstruction across the electrode cross-section is utilized to assess the spatial occurrence of cracks throughout the electrode thickness. Figures 3(a) and (b) present the distribution of gray scale values of the active material, derived from the reconstruction, as a function of the distance from the current collector. The pristine electrode in Figure 3(a) displays a narrow and homogeneous distribution of gray scale values across the electrode cross-section. Conversely,

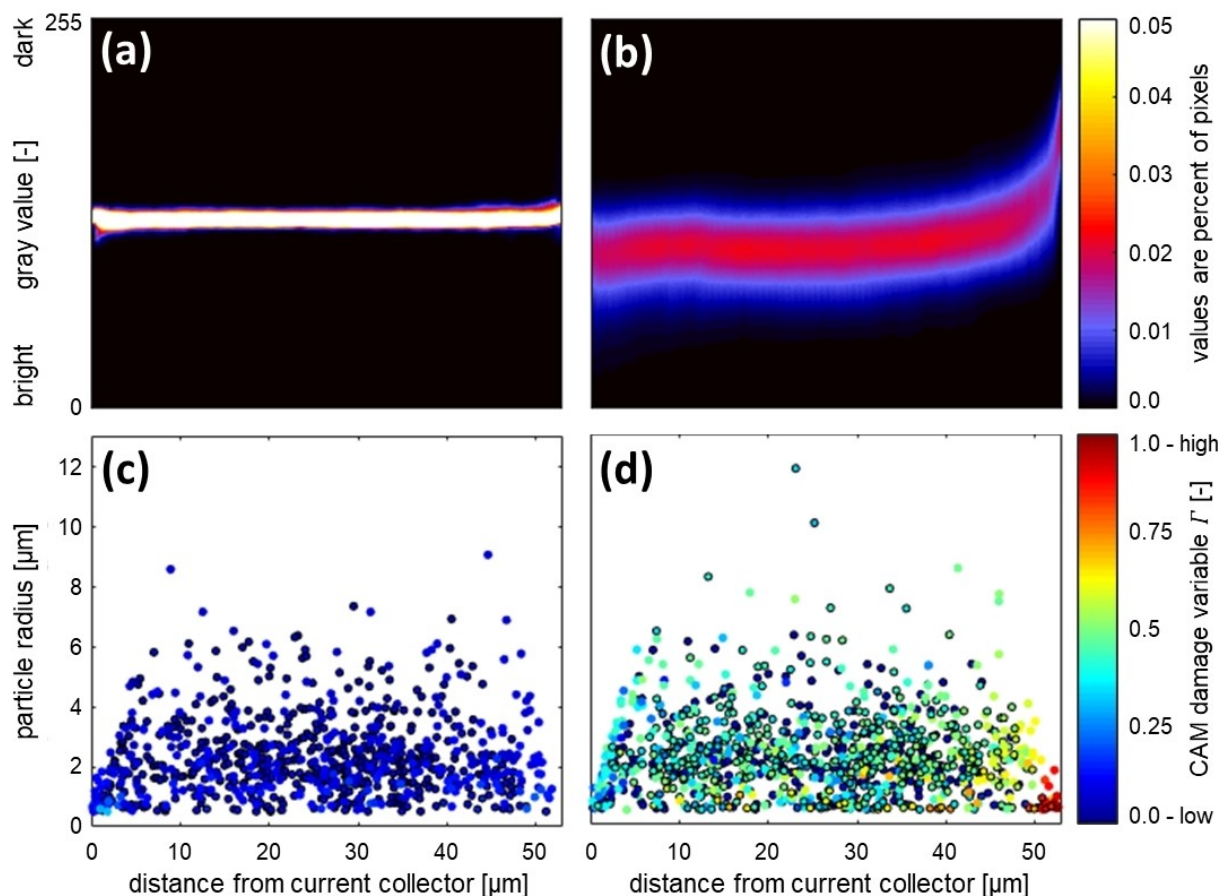


Figure 3. Particle density based on the gray scale value distribution as a function of the distance from the current collector, (a) pristine (0 cycles), (b) after 235 cycles. Particle radius and relative crack density as a function of the distance of the particles geometric center position from the current collector, (c) pristine (0 cycles), (d) after 235 cycles. The color codes represent the CAM damage variable Γ . Particles that were fully captured by the field of view of the nano-XCT scan are framed with a black circle.

the cycle-aged electrode in Figure 3(b) exhibits a broader distribution and a notable shift towards darker gray scale values in the region proximate to the separator interface. The correlation between gray values and cracking indicates that the pristine sample consists of uniformly dense particles throughout the entire electrode thickness. In contrast, the cycle-aged sample contains a higher proportion of cracked particles, particularly in the vicinity of the separator interface.

In the following, we analyze whether crack formation is homogeneously distributed over large and small particles, or whether some particle sizes are more prone to fracture. Further, their location within the electrode is analyzed. A homogeneous particle size distribution across the electrode cross-section is visible for the pristine electrode (see Figure 3(c)) and for the aged electrode (see Figure 3(d)). Thus, no accumulation of large or small particles may be made responsible for inhomogeneous cracking. To assess the relationship between particle size and crack formation, we utilize the CAM damage variable Γ_i , which is represented by different colors for individual particles. In Figure 3(c), the pristine electrode displays a low value of Γ across the entire electrode cross-section for all particle sizes. Conversely, Figure 3(d) shows an increase in crack density with increasing distance from the current collector, as indicated by

the damage variable Γ for the cycle-aged electrode. These findings align with the qualitative observations from SEM analysis and the gray scale values depicted in Figure 3(a–b). However, the identified morphological changes so far have mainly focused on descriptive parameters of the particle interior, while external changes have been barely detectable with the methods used in this section. Therefore, a targeted expansion of the characterization of the external geometric properties of the particles is of increased interest in the further course of the analysis, in order to provide a comprehensive description of the particle conditions and enable comparisons with other studies.

The occurrence of spatially heterogeneous crack formation was unexpected, considering the relatively moderate current rate of $C/2$ and a CV phase with a cut-off current of $C/20$ selected for the cycle experiment. These differences may be attributed to variations in the depth of discharge and the resulting stress on the active material across the electrode thickness. The non-uniform utilization of the CAM across the electrode thickness can be caused by either electrical or ionic limitation. According to Jiang et al., an electrical limitation occurs only when the particles are approximately 75% detached from the carbon binder matrix, resulting in a loss of

contact.^[22] Prior to reaching this threshold, typically only an ionic limitation is present. Hence, an ionic pathway limitation appears more likely, resulting in particles near the separator being heavily favored both at the beginning of life and throughout the cycle life. It should be noted that a direct comparison with the specific binder content and structural parameters investigated by Jiang et al. is not feasible in this study, but their findings are used for subsequent discussions. In the charging direction, concentration gradients in the active material are reduced by a very low cut-off current, which ensures uniform lithiation at high voltage levels. According to the literature, the mechanical stress induced by the volume change at high voltage levels is the main cause for crack formation.^[27,28] In our study, the discharge process involves constant current until reaching the cut-off voltage. Consequently, spatial deviations in concentration levels within the particles occur towards the end of discharge. Ionic limitations contribute to higher lithiation levels in particles near the separator compared to those closer to the current collector, resulting in an inhomogeneous depth of discharge across the electrode thickness. Particularly, particles located in proximity to the separator interface experience a higher cumulative charge throughput at low voltage levels. Over the cycle life, this cumulative volume change becomes more significant and appears to have a pronounced effect on crack formation.

Furthermore, it is noteworthy that the CAM damage variable Γ tends to be higher for small and medium-sized particles. This finding is intriguing since one would expect larger particles to exhibit more pronounced signs of CAM damage, considering their substantial volume changes during cycling. The accumulation of mechanical stress in larger particles could potentially lead to particle cracking. However, an explanation for the counterintuitive observation that small particles experience more cracking can be attributed to their higher surface-to-volume ratio compared to larger particles. This ratio can result in a greater cumulative charge throughput over the cycle life for small and medium-sized particles. Specifically, the smaller diameter allows for faster diffusion of lithium from the particle surface to its center. In contrast, a larger particle diameter can cause pronounced lithium concentration gradients in the active material. Such a steep gradient of lithium concentration may reduce stresses within the particle because of the accumulation of lithium near the particle surface while a large fraction of the particle remains less lithiated.^[29] Over the cycle life, this difference in lithium distribution may lead to a higher utilization of active material in small and medium-sized particles compared to larger particles. Consequently, the cumulative stress experienced by these particles becomes more significant, potentially resulting in increased cracking.

The CAM damage variables Γ , introduced in this study, can serve as a useful tool for comparing the mechanical degradation among different samples. Therefore, Γ is quantitatively assessed in the following by its cumulative distribution function and histogram for both the pristine and cycle-aged samples. Figure 4(a) depicts the Cumulative Distribution Function (CDF) for these samples. For the pristine sample, it is observed that over 95% of the particles have a CAM damage variable Γ below

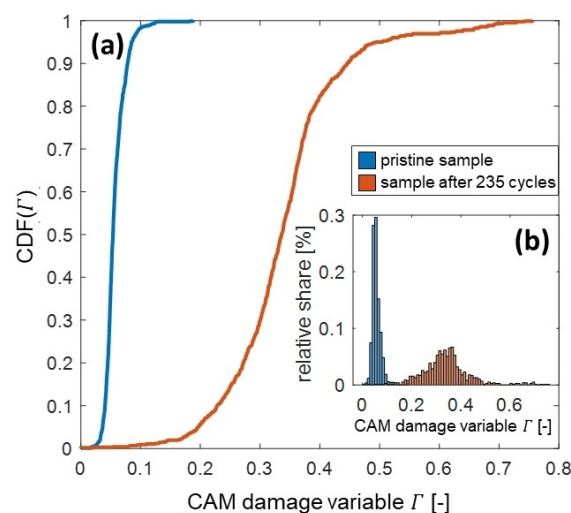


Figure 4. (a) Cumulative Distribution Function (CDF) of the computed relative crack density values for the pristine sample (blue) and the cycle-aged sample (orange). (b) Histogram of the computed relative crack density values for the pristine sample (blue) and the cycle-aged sample (orange).

0.1, with the remaining particles falling below 0.2. This confirms the low cracking rate for the pristine cell. In contrast, approximately 95% of the particles in the cycle-aged sample exhibit a CAM damage variable Γ above 0.2, indicating the presence of mechanical damage in almost all particles. The corresponding histogram, presented in Figure 4(b), illustrates the distribution of calculated CAM damage variable Γ values for both samples. In the case of the pristine sample, the values are tightly clustered around the mean, resulting in a narrow distribution. This indicates a relatively uniform level of the CAM damage variable Γ across all particles in the sample. In contrast, the distribution for the cycle-aged sample is broader and shifted towards higher values. Notably, outliers in the range of 0.6 to 0.75 represent particles located near the separator interface, displaying particularly pronounced signs of active material degradation. These results are in line with the previously made observations and provide an opportunity to quantitatively compare the mechanical damage in the particle interior among different electrode samples. Furthermore, it allows for the ordinal ranking of these samples based on their respective damage levels.

Following the preceding section, which focused on quantifying crack formation, particle size, and spatial position, the subsequent analysis focuses on the external geometric properties of the particles. Xu et al. and Lu et al. have raised concerns regarding the validity of cathode models based on ideal spherical particle geometry.^[9,29] Lu et al. observed a wide sphericity distribution and noted that cyclic aging may further decrease the spherical shape due to microstructure degradation.^[29] Figures 5(a) and (b) present the sphericity Ψ_{Lu} according to Lu et al. for the pristine (left) and aged (right) electrode as a function of the normalized long and short axis. Both electrodes predominantly exhibit medium to high sphericity for particles fully captured within the CT scan field of view. The broad sphericity distribution, previously observed by Lu

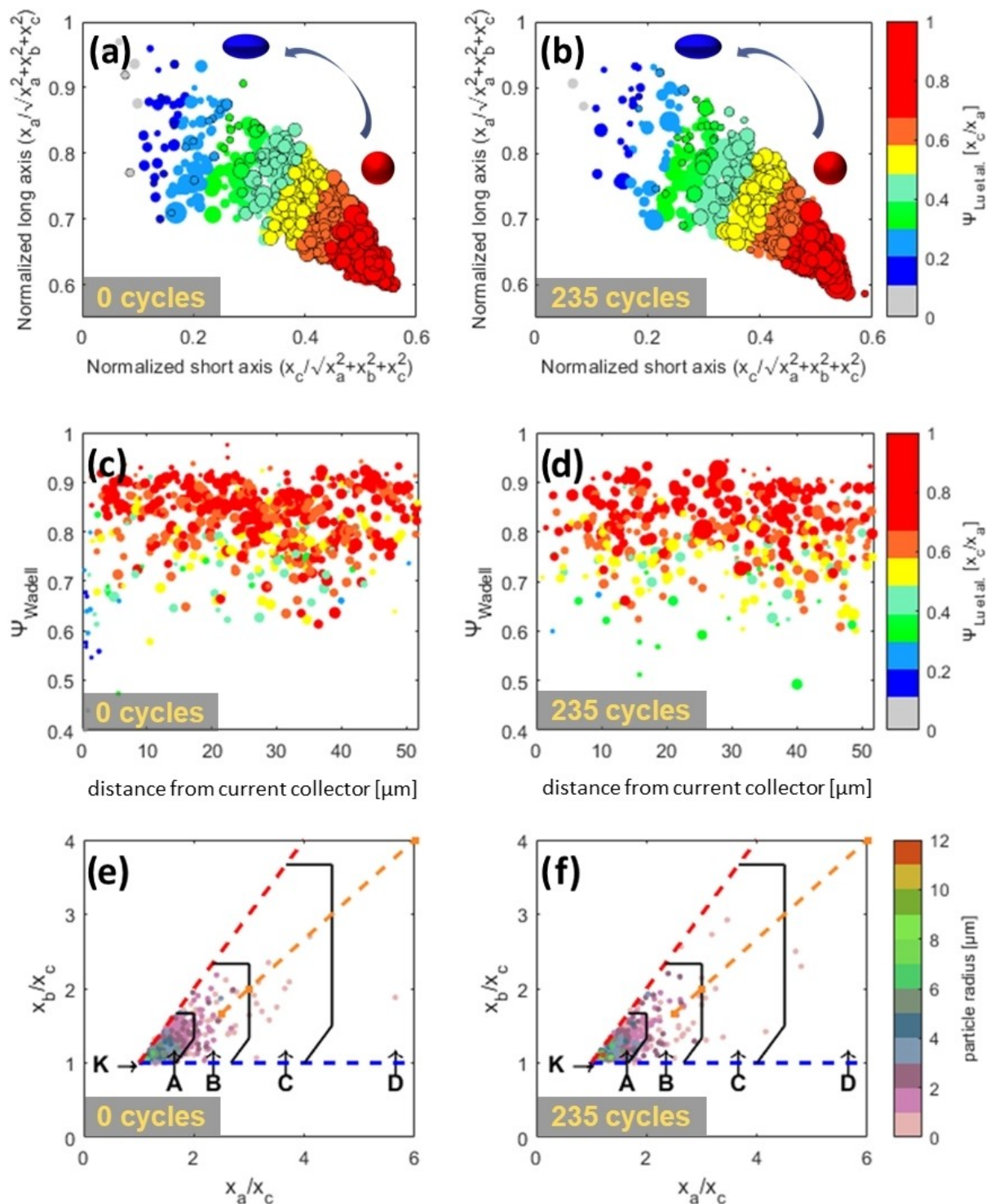


Figure 5. Sphericity analysis for pristine (a, c, e) and 235 cycle aged electrode (b, d, f). Sphericity distribution of the NMC particles for (a) pristine and (b) 235 cycle aged electrode. Particles that were not fully captured by the field of view of the nano-XCT scan are framed without a black circle. The size of the scatter points represents the radius of the particles. Sphericity according to Lu (2020) (x_c/x_a ratio) and sphericity according to Wadell (1935) as a function of the distance from the current collector for (c) pristine and (d) 235 cycle aged electrode. Shape diagram of the NMC particles according to Walz (1936), (e) pristine and (f) 235 cycle aged electrode; K: Ideal sphere; A: Very spherical shape; B: Compact, but not a pronounced spherical shape; C: Round and oblong geometry (cylinder); D: Round and extremely elongated geometry (needle-shaped); geometries above the orange line correspond to planar geometry (sheets). Please note that particles only partially captured are excluded in (c-f).

et al., mainly arises from particles that were not entirely captured in the field of view, resulting in a flattened geometric

shape.^[29] As these partially captured particles do not accurately represent reality, they are excluded from further analysis.

Furthermore, the sphericity Ψ_{Lu} , according to Lu et al. generally yields high sphericity values for compact particles of various shapes, such as a cube.

As depicted in Figure 3(c) and (d), the distribution of particle sizes remains uniform across the electrode cross-section both before and after cyclic aging. To examine if this uniformity extends to sphericity, we analyze the sphericity values according to Lu et al. and Wadell as a function of the distance from the current collector foil in Figures 5(c) and (d). The sphericity distribution in both the pristine and aged cell samples remains uniform, even in the region near the separator interface where a considerable increase in crack density was observed in the aged sample. For the pristine sample, the average sphericity values based on the Wadell definition, denoted as Ψ_{Wadell} , were 0.7015 ± 0.1134 , while the sphericity values based on the Lu et al. (2020) definition, denoted as Ψ_{Lu} , were 0.6329 ± 0.1420 . In the aged sample, the mean sphericity according to the Wadell definition was 0.6942 ± 0.1079 , and according to the Lu et al. definition, it was 0.6345 ± 0.1342 . We conclude that despite observing significant crack formation within the particles, no quantitative change in particle sphericity was observed based on both definitions. Further, the Wadell definition yielded higher average values with lower standard deviation compared to Lu's sphericity. From a visual inspection of Figure 5(c) and (d), the Lu et al. definition exhibited no correlation with Ψ_{Wadell} between sphericity values ranging from 0.6 to 1. However, no distinct trend in sphericity values was observed across the electrode thickness for both definitions. It is important to note that when particles are solely examined externally, for example, through micro-CT analysis at lower resolutions without the ability to assess the particle interior, this would erroneously suggest the absence of significant particle fragmentation. Particles exhibiting a very low sphericity in the vicinity of the current collector interface are probably caused by the sample preparation.

To evaluate the suitability of a simplified geometry other than ideal spheres for the pristine and aged particles, we adopt a quantitative approach based on Walz.^[24] Figures 5(e) and (f) present a diagram that plots all particles based on the ratios of their long vs. short axis (X_a/X_c) and middle vs. short axis (X_b/X_c), allowing for classification into shape categories such as spheres, cylinders, sheets, or needles. The concentration of data points in areas A (very spherical shape) and B (compact, but not a pronounced spherical shape), situated in the bottom left corner of the diagram, indicates that the majority of particles exhibit a spherical to compact shape. Notably, larger particles (green to red color) demonstrate a higher degree of sphericity, while smaller particles display greater deviations. In the aged electrode, a few small particles deviate from compactness, potentially representing fragments resulting from particle cracking. However, no significant differences are observed between the electrodes. In the pristine sample, approximately 82.9% of all particles are classified in area A, while an additional 14.5% of the particles fall into area B. In the cyclic aged sample, approximately 82.6% of all particles are categorized in Field A, with an additional 15.4% of the particles falling into Field B. Thus, indeed no change in shape or sphericity could be

detected. This result implies also that ideal spheres are the most suitable description for the aged particles, offering valuable insights for modelling aged electrodes using simplified microstructure models.

We can conclude so far that the observed particle cracking due to cyclic operation in the investigated electrode predominantly led to morphological changes in the interior of the particles. The particles did not pulverize, and the external geometric properties such as particle size alone are not indicative of performance degradation. Despite losing approximately 50% of its discharge capacity, the electrode maintained its shape. This finding has practical implications for modeling: considering the predominantly compact nature of the particles, even in the aged electrode, assuming ideal spheres remains the most suitable simplification for modeling NMC-based cathodes. However, the results also highlight the need for the utilization of sub-micrometer resolution CT devices for quantitative analysis of mechanical degradation in battery electrodes, enabling the assessment of the internal condition of the active material particles.

The method presented in this study offers an efficient approach for quantifying the mechanical degradation in battery active materials through the utilization of nano-XCT analysis. This technique provides a valuable tool for investigating a wide range of research questions that require a comprehensive understanding of the geometric properties of the active material particles. Moreover, it facilitates correlation analysis with other measurable quantities, such as electrical data, to gain deeper insights into the relationship between mechanical damage and various performance indicators. For instance, it allows for the selection of samples at different time points within a time series, enabling a quantitative tracking of the mechanical damage progression throughout the entire experiment. Furthermore, it can be used to rank different CAM optimization approaches or materials in an ordinal manner based on their damage levels. This ranking enables quantitative decision-making when determining development paths.

Conclusions

This work presented a computationally efficient analysis method based on nano-XCT for batteries, enabling quantitative insights into polycrystalline cathode active material and the ability to trace morphological changes after cycle aging. The aged cell has suffered a significant capacity loss of around 55% after cycling. The obtained results confirmed the initial observations from SEM images, emphasizing that particle cracking in the NMC811 electrode, induced by cycling, is most severe for particles located near the separator interface. This cracking phenomenon persisted despite implementing a moderate charging protocol, suggesting an inhomogeneous lithium concentration across the electrode thickness at the end of discharge as a potential cause. This is presumably the result of an inhomogeneous lithium concentration level across the electrode thickness at the end of discharge. In addition, it was found that the severity of the degradation is inhomogeneous

across different particle sizes. Smaller particles displayed more severe aging effects compared to larger particles. This finding highlights the importance of considering particle size when investigating the aging behavior of cathode active materials. While significant morphological changes were observed within the particle's interior, the quantitative analysis of the external particle geometry after cyclic aging using various approaches from the literature has shown that the changes in particle shape, size and sphericity due to mechanical degradation is negligible for the investigated electrode. This highlights the need for CT devices with sub-micron resolution in damage analysis of active material particles to access sub-surface degradation.

The proposed methodology for quantifying cracking and change in particle size and sphericity over the electrode cross-section was successfully applied to the pristine and the aged electrode sample. Based on our results, we postulate that the developed quantification method can be applied to various cathode and anode materials, provided that the particle size falls within the micrometer range. The ability to assess cracking and changes in particle characteristics offers valuable insights into the degradation mechanisms of different electrode materials. Furthermore, we propose nano-XCT as the standard method instead of micro-CT for analyzing damage in Ni-rich NMC electrodes, as it allows for the detection and quantification of internal cracks, which significantly impact the electrode performance. This recommendation arises from the observation that the decline in discharge capacity of ca. 55% cannot be solely attributed or detected by analyzing particle shape and sphericity. Instead, it is predominantly associated with the presence of internal cracks, which can be detected and quantified using nano-XCT. These findings underscore the need for further investigations into the properties of these damaged particles and their influence on key performance aspects such as electrical conductivity, charge transfer, and diffusivity.

The presented new and quantitative method will help to trace the aging process of Ni-rich NMC-based cathodes better and quantitatively evaluate new strategies to prevent structural degradation, which is essential for further commercialization. Directions for future work include quantitative tracking of crack formation resolved over the cycle life under various operating parameters.

Experimental Section

Materials

The polycrystalline NMC811 cathode active material explored in this work was purchased as an electrode sheet with a thickness of 70 μm including an 18 μm Al foil (3.0 mAh cm^{-2}) from a commercial supplier (Novonix Ltd., Canada). The selection of the electrode material intentionally avoided optimizations, such as doping or coatings, to preserve the inherent damage mechanisms associated with nickel-rich NMC. The cathode was punched to a diameter of 18 mm and assembled in a PAT half-cell from EL Cell with the so-called PAT Core system using lithium metal as the anode and a Whatman GF glass fiber separator (uncompressed thickness = 260 μm) under a protective argon atmosphere. 200 μL of BASF LP30

(1 mol LiPF_6 and ethylene carbonate/dimethyl carbonate (EC:DMC, 50:50 wt%)) with 2 wt% vinylene carbonate was used as the electrolyte.

Electrochemical cycling

The cell was initially subjected to a three-cycle CC–CV/CC–CV (constant current (CC), constant voltage (CV)) formation process with a constant current density of 0.286 mA cm^{-2} ($\sim\text{C}/10$ rate) and a cut-off current of 0.143 mA cm^{-2} ($\sim\text{C}/20$ rate) at the end of the CV phase. In addition, a slow discharge capacity test at a low current rate of C/20 was conducted before and after the cycle test. For the cyclic aging test, a total of 235 cycles of CC–CV/CC were performed at a constant current density of 1.43 mA cm^{-2} ($\sim\text{C}/2$ rate) and at a temperature of 25 °C. The voltage range for the cycling was set between 3.0 and 4.35 V. During the CV step, a low cut-off current of 0.143 mA cm^{-2} ($\sim\text{C}/20$ rate) was applied at the end of charge to minimize Li concentration gradients within the electrode, ensuring a homogeneous utilization of the entire active material. Following the completion of the cyclic aging test, the cell was discharged to 3.0 V and disassembled within a glove box. The positive electrode was extracted and washed with dimethyl carbonate to remove solvent and conductive salt residues. The electrode was then subjected to post-mortem analysis using scanning electron microscopy and nano X-ray computed tomography.

Scanning electron microscopy

SEM images were captured using a ZEISS GeminiSEM 360 electron microscope. The imaging process involved acquiring images of both a pristine electrode sample and a washed and dried electrode sample, employing an accelerating voltage of 5.0 kV and a current of 200 pA. The preparation of cross-sections on the electrode samples was carried out using an ion milling process facilitated by a Hitachi ArBlade 5000 ion milling system operating at an acceleration voltage of 8 kV. The duration of the ion milling procedure was set to 3 hours.

Nano X-ray computed tomography

Nano-XCT scans were recorded on samples from the same electrodes using a laboratory-based X-ray microscope (Xradia, nano-XCT-100, Xradia Inc. Pleasanton, CA, USA) with a photon energy of 8 keV in absorption contrast mode. The imaging was conducted with a field of view measuring 66.5 x 66.5 μm^2 and a resolution of 1024 x 1024 pixels per image. The attenuation length for NMC811 at 8 keV exceeds 200 μm , while for the Al-foil, it measures approximately 75 μm , making the electrode thickness well-suited for the field of view and providing reasonable absorption contrast. To achieve a triangular sample shape, the second direction was prepared using surgical scissors. The narrow apex of this triangle possesses a width only slightly larger than the field of view, ensuring effective X-ray transmission. It's important to note that any damaged portions were excluded from the tomographed volume. A complete set of tomographic data comprising 801 images was acquired over a 180° rotation (parallel beam geometry), with an exposure time of 180 s for each image (see Figure 1(a)). The inherent stability of the nano-XCT machine ensures minimal sample movement during scanning. To compensate for slight stage variations, a spherical fiducial gold marker was strategically placed within the sample. This marker's position was continuously monitored, enabling image realignment before reconstruction. These images were aligned using a custom plugin in Fiji/ImageJ and subsequently reconstructed using weighted back-projection from the software Tomo3D.^[30,31] The X-ray CT scans covered the electrode samples from the current collector

to the separator interface with a resolution of 0.35 $\mu\text{m}/\text{voxel}$. This high resolution provided detailed insights into the electrode morphology. Finally, the 1024 sliced images were assembled to generate a three-dimensional reconstruction of the actual electrode, as illustrated in Figure 1(b–c).

The nano-XCT data was segmented by pixel classification with the software *ilastik*.^[32] Subsequently, data analysis was carried out using the software in *Fiji/ImageJ* using procedures of various plugins (*BoneJ*, *MorphoLibJ*, *3DSuite*).^[33–35] The particle volume was split into individual particles by a 3D distance transform watershed algorithm to avoid over-segmentation, as shown in Figure 1(d), allowing evaluation of the individual particles. The particle volume was then determined for each particle and the equivalent particle radius was calculated assuming an ideal sphere. All CAM particles with a volume bigger than $1\ \mu\text{m}^3$ were classified into either complete particles or partial particles for particles that are cut by the border of the cylindrical reconstruction volume. The signal-to-noise ratio (SNR) in laboratory-based nano-XCT is acknowledged to be generally less favorable when compared to synchrotron nano-XCT or conventional micro-CT. This disparity in SNR arises from the inherent constraints of laboratory-based setups. However, in terms of image assessment, the contrast-to-noise ratio holds greater significance; it delineates the signal separation from the foreground (NMC) to the background (rest) in relation to the noise. Typically expressed as contrast-to-noise ($\text{CNR} = \frac{\text{signal}_A - \text{signal}_B}{\text{std. deviation}_B}$), this metric offers a robust measure. Specifically, the CNR between the NMC811 material segment class and the class denoting the volume between NMC811 particles, excluding foil, air, and gold fiducial in the tomography data exhibits a value of ~ 2 .

Figure 1(e) shows a 2D slice of the 3D reconstruction of a CT scan across the electrode thickness, including the current collector and the active material particles with different degrees of fracture. While larger cracks in the CAM particles with an opening of approximately 300 nm and more can be detected directly in the CT data, more minor cracks are not resolved. However, the gray scale value in a voxel that contains small cracks is darker compared to voxels containing dense CAM material. To make this information on small cracks mathematically usable for further analysis, the gray scale values of the tomography images are used. The gray scale values are given on a unitless scale from 0 to 255, where 0 stands for completely black and 255 for pure white. Any value in between corresponds to a certain degree of gray and can be interpreted accordingly as crack density in the CAM for the present data. The lower the mean gray scale value in the section of the CAM under consideration, the higher the proportion of darker voxels or the proportion of cracks in the CAM, as already observed in the work of Rahe et al. and Yang et al.^[10,20] Conversely, the higher the mean gray scale value, the lower the proportion of cracks in the CAM. This circumstance is leveraged in this study to formulate a heuristic, whereby the mean gray scale value of each CAM particle is determined and used as a measure for quantifying the damage caused by cracks. To mitigate the influence of factors such as lighting conditions and facilitate the comparison of CT scans, the mean gray scale value of each CAM particle is subsequently normalized. This normalization is achieved by calculating $G_{\text{normalized},i} = \frac{G_{\text{raw},i}}{G_{\text{dense CAM}}}$, where $G_{\text{raw},i}$ represents the mean gray value of the particle i , and $G_{\text{dense CAM}}$ is obtained as the average mean gray scale value among the three densest CAM particles within the reconstructed volume. These three particles exhibit the highest mean gray scale value and have a minimum radius of 2 μm . The selection of the three densest particles forms a reference for dense CAM. Through the adopted approach, it inherently guarantees the preferential selection of particles exhibiting minimal internal pores or cracks. As a result, in our heuristic algorithm, all particles in the sample are evaluated against the reference set by the mean gray

scale value of the three densest particles. Particularly small particles, typically spanning only a few micrometers and comprising just a few or single primary particles, commonly lack intergranular cracks or internal pores. This feature renders them consistently dense and highly appropriate as a reference. The degree of fracture due to cracking is calculated for each particle i as CAM damage variable $\Gamma_i = 1 - \frac{G_{\text{normalized},i}}{\max(G_{\text{normalized},i})}$. Consequently, the CAM damage variable Γ_i is rescaled to a range spanning from zero (indicating the reference value for dense CAM with minimal indications of crack formation within the electrode sample) to one (representing an upper limit for the utmost theoretically achievable crack formation). The value of one can solely be theoretically attained if a particle is entirely hollow, with its interior exclusively comprising black voxels. It should be noted that the newly introduced variable Γ_i serves as a proxy value, capturing the damage extent of each particle i relative to a reference established by the three most dense particles within the electrode sample. Particularly, Γ_i does not directly represent the physical crack density but offers a precise assessment of a particle's damage level in relation to the reference particles. This scaling technique serves as a straightforward heuristic, facilitating an easy comparison of crack-related damage among different particles, their position along the electrode thickness and even across different electrode samples.

This approach, which is easy to implement and calculate, allows a spatially resolved quantification of the morphological changes of the CAM particles after the cycling experiment. For example, a CAM particle with high crack density will inevitably show a higher proportion of darker gray scale value voxels in the reconstruction, resulting in a lower mean gray scale value of the particle. As a result, the high ratio of dark to light voxels leads to a higher value of CAM damage variable Γ for the particle. This proxy value simplistically represents the physical crack density, which is calculated as the ratio of voxels marked as cracks to voxels marked as CAM and requires the application of a computationally intensive segmentation algorithm. However, a time-consuming procedure for precise segmentation and labeling of the cracks can be omitted. In the subsequent section, we conduct a comprehensive analysis that encompasses both crack density within the particles and a quantitative assessment of their external geometric properties. This includes size, shape, spatial distribution within the electrode thickness, and a simplified geometric characterization. To our knowledge, this study represents the first extensive analysis of this nature conducted on electrode samples, comparing a pristine sample with an aged counterpart.

Author Contributions

Daniel Goldbach: writing – original draft, conceptualisation, data curation, visualisation, formal analysis, investigation. **Jurgen Gluch:** Data curation: Supporting; Methodology: Supporting. **Tanja Graf:** Supervision: Supporting. **Michael Gaus:** Supervision: Supporting. **Stefan Kabitz:** Supervision: Supporting. **Michael Zillmer:** Supervision: Supporting. **Ulrike Krewer:** Conceptualisation, Supervision, Supporting, writing – review & editing.

Acknowledgements

The authors acknowledge the financial support provided by Volkswagen AG and the technical realization assistance pro-

vided by Fraunhofer IKTS. Open Access funding enabled and organized by Projekt DEAL.

Conflict of Interests

The authors declare no conflict of interest.

Data Availability Statement

The data presented in the manuscript are openly available in the KITopen repository at doi: 10.35097/1734.

Keywords: Aging · Particle cracking · 3D reconstruction · Spatial resolution of morphological changes · Graphical evaluation

- [1] G. Blomgren, *J. Electrochem. Soc.* **2017**, *164*, A5019–A5025.
- [2] J.-M. Tarascon, *Phil. Trans. R. Soc. A* **2010**, *368*, 3227–3241.
- [3] W. Li, E. Erickson, A. Manthiram, *Nat. Energy* **2020**, *5*, 26–34.
- [4] A. Manthiram, B. Song, W. Li, *Energy Storage Mater.* **2017**, *6*, 125–139.
- [5] Q. Wu, S. Mao, Z. Wang, Y. Tong, Y. Lu, *Nano Select* **2020**, *1*, 111–134.
- [6] H.-H. Ryu, K.-J. Park, C.-S. Yoon, Y.-K. Sun, *Chem. Mater.* **2018**, *30*, 1155–1163.
- [7] P. Teichert, G. G. Eshetu, H. Jahnke, E. Figgemeier, *Batteries* **2020**, *6*, 8.
- [8] P. J. Withers, *Mat. Today* **2007**, *10*, 26–34.
- [9] E. Maire, P. J. Withers, *Int. Mater. Rev.* **2013**, *59*, 1–43.
- [10] T. M. M. Heenan, C. Tan, J. Hack, D. J. L. Brett, P. R. Shearing, *Mat. Today* **2019**, *31*, p. 69–85.
- [11] Z. Su, V. D. Andrade, S. Cretu, Y. Yin, M. J. Wojcik, A. F. Alejandro, A. Demortière, *ACS Appl. Energ. Mater.* **2020**, *3*, 4093–4102.
- [12] P. Pietsch, V. Wood, *Annu. Rev. Mater. Res.* **2017**, *47*, 451–479.
- [13] S. Müller, M. Lippuner, M. Vezhzhak, V. D. Andrade, F. D. Carlo, V. Wood, *Adv. Energy Mater.* **2020**, *10*, 2070120.
- [14] C. Tan, T. M. M. Heenan, R. F. Ziesche, S. R. Daemi, J. Hack, M. Maier, P. R. Shearing, *ACS Appl. Energ. Mater.* **2018**, *1*, 5090–5100.
- [15] M. Ebner, D.-W. Chung, R. E. García, V. Wood, *Adv. Energy Mater.* **2013**, *4*, 1301278.
- [16] T.-T. Nguyen, J. Villanova, Z. Su, R. Tucoulou, B. Fleutot, B. Delobel, C. Delacourt, A. Demortière, *Adv. Energy Mater.* **2021**, *11*, 2003529.
- [17] T. M. M. Heenan, A. V. Llewellyn, A. S. Leach, M. D. R. Kok, C. Tan, R. Jervis, D. J. L. Brett, P. R. Shearing, *Adv. Sci.* **2020**, *7*, 2000362.
- [18] R. Xu, Y. Yang, F. Yin, P. Liu, P. Cloetens, Y. Liu, *J. Mech. Phys. Solids* **2019**, *129*, 160–183.
- [19] Y. Yang, R. Xu, K. Zhang, S.-J. Lee, L. Mu, P. Liu, *Adv. Energy Mater.* **2019**, *9*, 1900674.
- [20] C. Rahe, T. Kelly, R. Stephen, N. Mansoureh, D. U. Sauer, J. Mayer, E. Figgemeier, *J. Power Sources* **2019**, *433*, 126631.
- [21] Z. Su, E. Decencièrre, T.-T. Nguyen, E.-A. Kaoutar, V. D. Andrade, A. F. Alejandro, *Comput. Mater.* **2022**, *8*, 30.
- [22] Z. Jiang, J. Li, Y. Yang, *Nat. Commun.* **2020**, *11*, 2310.
- [23] X. Lu, A. Bertei, D. P. Finegan, C. Tan, S. R. Daemi, J. Weaving, S. Julia, *Nat. Commun.* **2020**, *11*, 2079.
- [24] K. Walz, *Die Bestimmung der Kornform der Zuschlagstoffe*, Hg. v. *Betonstraße 11.2*, **1936**, p. 27–32.
- [25] H. Wadell, *J. Geol.* **1935**, *43*, 250–280.
- [26] P. Teichert, H. Jahnke, E. Figgemeier, *J. Electrochem. Soc.* **2021**, *168*, 090532.
- [27] P. Yan, J. Zheng, M. Gu, J. Xiao, J.-G. Zhang, C.-M. Wang, *Nat. Commun.* **2017**, *8*, 14101.
- [28] A. O. Kondrakov, A. Schmidt, J. Xu, H. Geßwein, R. Mönig, P. Hartmann, *J. Phys. Chem.* **2017**, *121*, 3286–3294.
- [29] R. Xu, L. S. De Vasconcelos, J. Shi, J. Li, K. Zhao, *Exp. Mech.* **2018**, *58*, 549–559.
- [30] J. Schindelin, I. Arganda-Carreras, E. Frise, V. Kaynig, M. Longair, T. Pietzsch, *Nat. Methods* **2012**, *9*, 676–682.
- [31] J. I. Agulleiro, J. J. Fernandez, *Bioinformatics* **2011**, *27*, 582–583.
- [32] S. Berg, D. Kutra, T. Kroeger, C. N. Straehle, B. Kausler, C. Haubold, *Nat. Methods* **2019**, *16*, 1226–1232.
- [33] M. Doube, M. M. Klosowski, I. Arganda-Carreras, F. P. Cordelières, R. P. Dougherty, J. S. Jackson, *Bone* **2010**, *47*, 1076–1079.
- [34] D. Legland, I. Arganda-Carreras, P. Andrey, *Bioinformatics* **2016**, *32*, 3532–3534.
- [35] J. Ollion, J. Cochennec, F. Loll, C. Escudé, T. Boudier, *Bioinformatics* **2013**, *29*, 1840–1841.

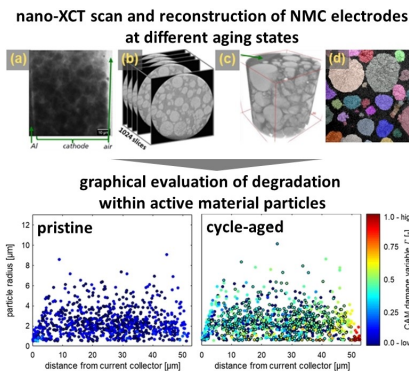
Manuscript received: July 24, 2023

Revised manuscript received: September 11, 2023

Version of record online: ■■■■■

RESEARCH ARTICLE

Nano-XCT analysis for batteries: This study compares scanning electron microscopy images and nano X-ray computed tomography scans of pristine and cycle-aged battery electrodes. Structural changes over the cycle life are determined, and a quantitative analysis of the active material's gray scale value distribution reveals severe degradation near the separator interface, with a reciprocal relationship to particle radius.



*D. Goldbach, Dr. J. Gluch, Dr. T. Graf, Dr. M. Gaus, Dr. S. Käbitz, Dr. M. Zillmer, Prof. Dr.-Ing. U. Krewer**

1 – 12

An Efficient Approach for Quantifying the Mechanical Degradation of Ni-Rich NMC-based Cathodes for Lithium-Ion Batteries using Nano-XCT Analysis

